Tellus
SERIES B
CHEMICAL
AND PHYSICAL
METEOROLOGY
PUBLISHED BY THE INTERNATIONAL METEOROLOGICAL INSTITUTE IN STOCKHOLM

Tellus (2010), 62B, 181–189
Printed in Singapore. All rights reserved

TELLUS

Observational quantification of a total aerosol indirect effect in the Arctic

By DAN LUBIN[1]* and ANDREW M. VOGELMANN[2], [1]*Scripps Institution of Oceanography, University of California San Diego, La Jolla, CA 92093–0221, USA;* [2]*Brookhaven National Laboratory, Upton, NY 11973, USA.*

(Manuscript received 2 July 2009; in final form 14 April 2010)

ABSTRACT

We use 6 yr of multisensor radiometric data (1998–2003) from the U.S. Department of Energy Atmospheric Radiation Measurement (ARM) program to provide an observational quantification of the short-wave aerosol first indirect effect in the Arctic. Combined with the previously determined long-wave indirect effect, the total (short-wave and long-wave) first indirect effect in the high Arctic is found to yield a transition from surface warming of +3 W m^{-2} during March to a cooling of –11 W m^{-2} during May, therefore altering the seasonal cycle of energy input to the Arctic Earth–atmosphere system. These data also reveal evidence of a first indirect effect that affects optically thinner clouds during summer, which may represent an additional negative climate feedback that responds to a warming Arctic Ocean with retreating sea ice.

1. Introduction

Aerosol-cloud interactions are a major source of uncertainty in current global climate change simulations that critically need direct observations to resolve (Penner et al., 2006). Northern high latitudes are showing some of the most dramatic manifestations of anthropogenic climate change (Stroeve et al., 2007) and recent work showed that springtime pollution aerosol act to enhance the downwelling long-wave radiation from Arctic clouds by altering their microphysics via a mechanism known as the first indirect effect (IDE_1), which yields enhanced surface long-wave fluxes comparable to those caused by CO_2 abundance increases (Lubin and Vogelmann, 2006; Garrett and Zhao, 2006). However, assessing the total IDE_1 depends on the concurrent impact at short wavelengths, as the Arctic insolation increases from zero during winter to a maximum at the vernal equinox. Here we determine the short-wave component of the IDE_1 in the Arctic utilizing the unique multiyear and multisensor data from the U.S. Department of Energy Atmospheric Radiation Measurement (ARM) program's North Slope of Alaska (NSA; 71°19'37.73"N, 156°36 56.70"W) site at Barrow (Stamnes et al., 1999). The result can serve as a benchmark climatological result against which climate model parametrizations can be tested.

*Corresponding author.
e-mail: dlubin@ucsd.edu
DOI: 10.1111/j.1600-0889.2010.00460.x

2. Methods

Pyranometer data from the NSA are used to determine the cloud transmission T_c, which is defined here as the ratio of the measured downwelling short-wave flux (insolation) at the surface to the equivalent surface flux under cloud-free skies and background aerosol (with all other atmospheric conditions constant). Pyranometer measurements (Michalsky et al., 1999) are made by the Sky Radiometers on Stand for Downwelling Radiation (SKYRAD) instrument suite. The broad-band surface albedo (α_{sw}) measurements are derived by ratio of these measurements with the upwelling flux made by the Ground Radiometers on Stand for Upwelling Radiation (GNDRAD) suite. Data used are recorded at 20 s and averaged to 1 min. The data used in this study encompass the years 1998–2003. Both suites are standard ARM program measurements kept in continuous operation at the NSA. To compute the cloud-free downwelling surface flux, F_{cf}, we use a 179-band discrete-ordinates radiative transfer model (Stamnes et al., 1988) optimized for the Arctic atmosphere (Lubin and Vogelmann, 2007), which corrects for the annual cycle in Earth-sun distance and incorporates spectral surface albedo for various Arctic conditions (Grenfell and Perovich, 1984; Perovich et al., 2002). F_{cf} is estimated using the following combinations of spectral surface albedos that are determined based on the measured value of α_{sw}: snow-covered sea ice for $\alpha_{sw} > 0.91$, a linearly weighted mixture of bare and snow-covered sea ice for $0.65 \leq \alpha_{sw} \leq 0.91$, a similar mixture of tundra and bare sea ice for $0.14 \leq \alpha_{sw} < 0.65$ and tundra for $\alpha_{sw} < 0.14$. These approximations are appropriate for a coastal high latitude station, given the spatial variability in multiple photon reflection

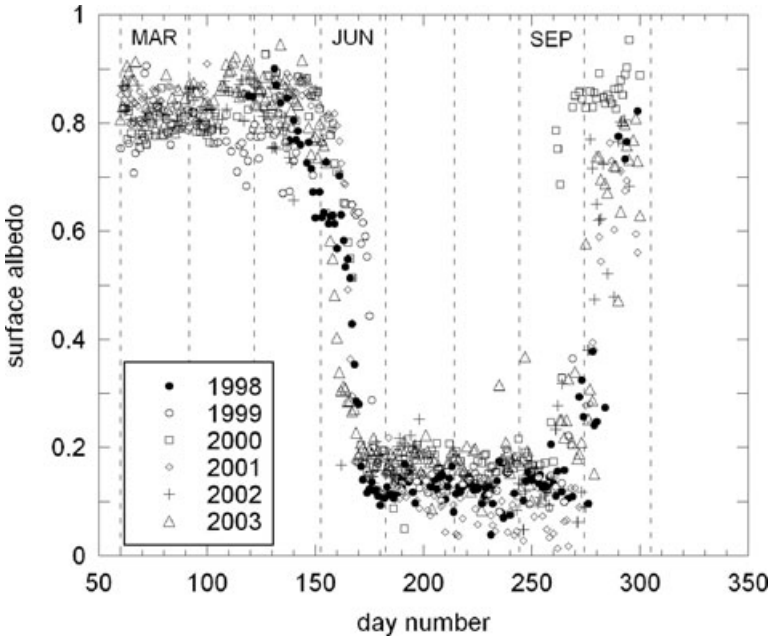

Fig. 1. Daily average broadband surface albedo measured at the ARM NSA site at Barrow, AK during 1998–2003. Vertical dashed lines identify the months.

effects for the full range of surface albedo (Podgorny and Lubin, 1998).

Before examining the differences between cloud transmissions under clean-air versus all other conditions, we need to account for any dependence on solar zenith angle θ_0. Solar zenith angle differences as small as 5° can yield differences in T_c comparable to those we expect from the IDE_1. Therefore, we examined the entire data set for solar zenith angle dependence, and derived a normalization $T_c = T_{c0} + a(0.5 - \mu_0)$, where T_{c0} is the uncorrected cloud transmission, $\mu_0 = \cos\theta_0$, and from a linear regression $a = 0.514$, 0.538, 0.473 and 0.620 for March–May, June, July–August and September–October, respectively. With the T_c values thus normalized to $\theta_0 = 60°$, we can search for a short-wave manifestation of the IDE_1 without worrying about possible artefacts from systematic differences in mean solar zenith angle.

Figure 1 shows the seasonal cycle in daily average α_{sw}. The albedo is uniformly high during spring until late May, when it begins to decrease with the onset of the melt season. The timing of the melt season and α_{sw} decrease varies considerably from one year to the next during June, as does the timing of the autumn freeze-up and α_{sw} increase during September and October. Based on this seasonal cycle in α_{sw}, we subdivide our analysis of IDE_1 into four time periods, (a) March–May, (b) June, (c) July and August and (d) September and October. During June, we only interpret the T_c determinations for which $\alpha_{sw} > 0.4$, when there are a sufficient number of data points.

The subset of Arctic clouds sampled herein was identified as being single-layered by the ARM Active Remotely-Sensed Cloud Locations algorithm (ARSCL; Clothiaux et al., 2000). Figure 2 shows T_c as a function of ARSCL-measured cloud base altitude. As expected, higher clouds are generally optically thinner. However from March to July, clouds with bases in the lowest part of the boundary layer have on average a slightly smaller optical thickness (and larger T_c) than those just above. The ARSCL data also reveal (not shown) that these lowest clouds have a tendency to be geometrically thinner than those just above, where 75% of them have a geometrical extent less than 500 m versus 65% for the clouds just above. Thus, with so many of these clouds contained within the boundary layer and also having relatively lower optical thickness, we can expect some degree of susceptibility to cloud nucleation (and concomitant changes in cloud radiative properties) from aerosol contained within the boundary layer. With the available data, only clouds having cloud base and cloud thickness both under 1000 m are used for statistical analysis of the IDE_1. (Due to various gaps in the pyranometer data set and the location's cloud climatology, there are considerably fewer determinations of T_c for higher clouds than for those below 1000 m.) This restriction of our IDE_1 analysis to the lowest clouds favours liquid water during the Arctic spring and summer. Figure 3 shows the distribution of base height and geometrical thickness for the clouds considered in our IDE_1 analysis. Most of these clouds are likely to be within the boundary layer, even during summer.

Measurements of downwelling zenith middle-infrared radiance from the Atmospheric Emitted Radiance Interferometer (AERI) (Knuteson et al., 2004) are used to retrieve cloud effective droplet radius, r_e and liquid water path, *LWP*, using established radiative transfer algorithms (Guo et al., 2005; Lubin and

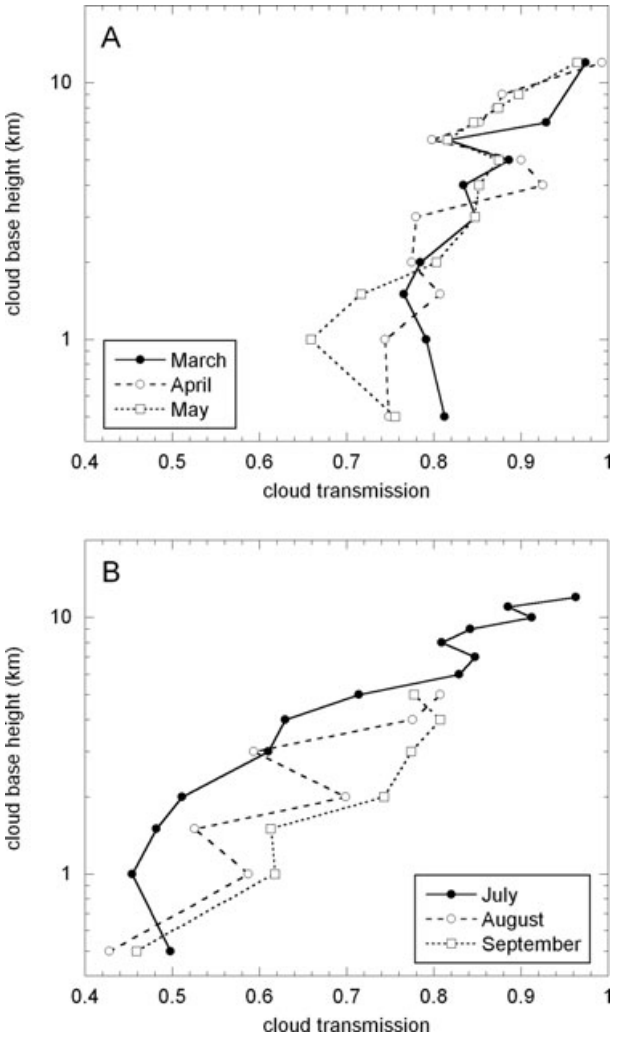

Fig. 2. Average cloud transmission T_c derived from the 1998–2003 NSA pyranometer data for single-layered clouds, as a function of cloud base altitude, during (A) spring and (B) summer and early autumn. Results for June are similar to those of May, and are omitted for clarity.

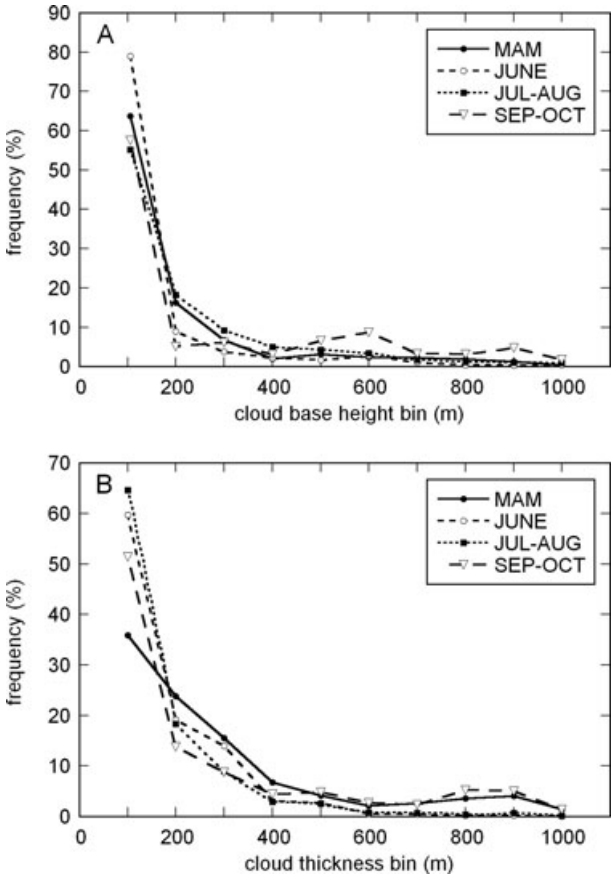

Fig. 3. Histograms of cloud base height (A) and cloud geometrical thickness (B), as determined from ARSCL data, for the cloud cases considered in this study.

Vogelmann, 2006). AERI-retrieved *LWP* and r_e are considered spurious if $LWP > 50$ g m^{-2}, due to lack of spectral variability in mid-IR cloud emission (Turner, 2005). For $LWP > 50$, r_e is not retrieved and *LWP* is specified from the microwave radiometer (MWR) data (Westwater et al., 2001). MWR data are, in turn, not reliable for smaller instantaneous *LWP* values due to large radiometric uncertainty (Westwater et al., 2001). To eliminate potential discontinuity at the merger of these two *LWP* retrievals, the MWR-retrieved *LWP* was regressed against the AERI-retrieved *LWP*. This revealed a bias and slope of 12.841 g m^{-2} and 1.092, respectively, in the MWR retrievals as compared to the AERI retrievals, and the bias was subtracted from all MWR *LWP* values.

3. Results

Several observational and theoretical studies have shown that anthropogenic aerosol in the Arctic troposphere, when entrained in clouds, decreases the effective radius r_e of cloud liquid water droplets (Morrison et al., 2005; Garrett and Zhao, 2006; Lubin and Vogelmann, 2006). The common occurrence of this IDE_1 for optically thin, low-level clouds at Barrow, AK can be seen using AERI retrievals of r_e and *LWP*. We collocate these retrievals with hourly-averaged measurements of aerosol condensation nuclei (CN) concentrations at Barrow (Delene and Ogren, 2002). During spring, CN can often serve as a proxy for cloud condensation nuclei (CCN) concentrations (e.g. Garrett et al., 2004). During summer, we do not expect a straightforward relationship between CN and CCN, as new particle formation by nucleation can yield large CN concentrations (of order 100–1000 cm^{-3}) that do not contribute to CCN, even though CCN concentrations of order 100 cm^{-3} can be observed sometimes during the Arctic summer (Garrett et al., 2004). In the absence of a clear relationship between CN and CCN during summer, we use the surface-measured CN concentrations as a simple discriminator

between pristine clean-air conditions (no measurable IDE_1 expected) and all other conditions, which may or may not contain CCN (and therefore may or may not exhibit an IDE_1). Here the natural background range is taken to be 0–50 cm^{-3}. Although higher CN does not necessary indicate high CCN during summer, we make the defensible assumption that, for low clouds, background CN concentrations implies background CCN concentrations.

Figure 4a shows that, in nearly all cases, r_e values decrease with increasing CN concentration above the natural background range of 0–50 cm^{-3}. Because this result prevails when we hold *LWP* nearly fixed (open circles in 4a), it is consistent with the IDE_1 (Twomey, 1977). The IDE_1 appears in optically thin clouds during the Barrow spring (Fig. 4a) and summer months (Figs. 4b and 4c), but is not perceptible during autumn (Fig. 4d). The summertime result is surprising given that the aerosol size distribution in the high Arctic typically exhibits a seasonal shift from having an accumulation mode dominate the distributions in spring and autumn to having a nucleation/Aitken mode dominate the summertime distribution (e.g. Garrett et al., 2004; Heintzenberg et al., 2006; Engvall et al., 2008), and therefore the relationship between surface-measured CN and CCN should be much less clear, as discussed above. Nevertheless, our result of Figs. 4b and c for the summer months appears when using two completely independent measurements—a surface particle counter for CN and spectroscoptic remote sensing retrieval for r_e—and remains to be explained.

One possibility is that this result is merely an artefact of airmass correlation, which has been shown to confound remote sensing-based identification of the IDE_1 (e.g. Mauger and Norris, 2007). If differences in CCN are mainly due to differences in prevailing wind direction and aerosol origin, and retrievals obtained from clouds in a moist airmass with high CCN (one wind direction) are arbitrarily juxtaposed with retrievals obtained from clouds in a less moist airmass with lower CCN (another wind direction), then an artificially strong IDE_1 will appear. We attempted to identify possible airmass correlation using the available NSA data. From surface meteorological observations in July and August, we identified two prevailing wind regimes, a westerly regime with wind directions 240°–320° and an easterly regime with wind directions 20°–100°. The former is accompanied by higher surface temperatures and lower surface pressures than the latter. Together, these regimes comprise 83% of the data containing the low clouds considered in this study. Figure 5 shows the observed inverse relationship between retrieved r_e and CN, for July and August, appearing for both wind regimes. The easterly regime overlaps with the preferred 'clean air' direction for air sampling at Barrow by NOAA (Polissar et al., 2001). Measurements made during westerlies might conceivably involve local pollution artefacts from Barrow, Alaska although, as a precaution, data points with wind direction within ±10° of the direction of Barrow (2 km distant) have been omitted from analysis. There appear to be systematic differences in

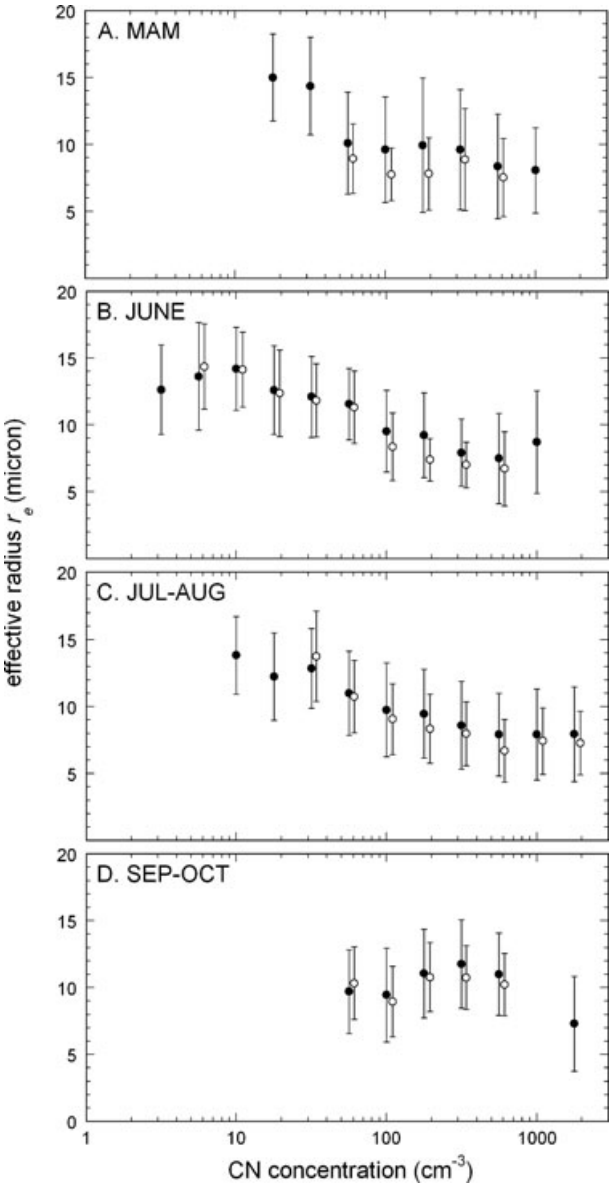

Fig. 4. Instantaneous AERI retrievals of r_e in low-level, optically thin (LWP < 50 g m^{-2}) stratiform cloud over Barrow, AK, from years 1998–2003 and for the months (A) March, April and May (MAM), (B) June, (C), July and August and (D) September and October, as a function of the corresponding CN hourly averaged concentration. The r_e retrievals are averaged over CN concentration bins whose outer bounds are specified in the plot. Vertical error bars are $\pm 1\sigma$. Solid points are the averages over all applicable data; open circles are the averages over the LWP range 5–15 g m^{-2}.

r_e between the two wind regimes, but a relationship between r_e and CN consistent with an IDE_1 appears with similar consistency for either regime. Thus, with the readily available NSA data, we find no obvious airmass correlation altering the result of Figs 4b and c.

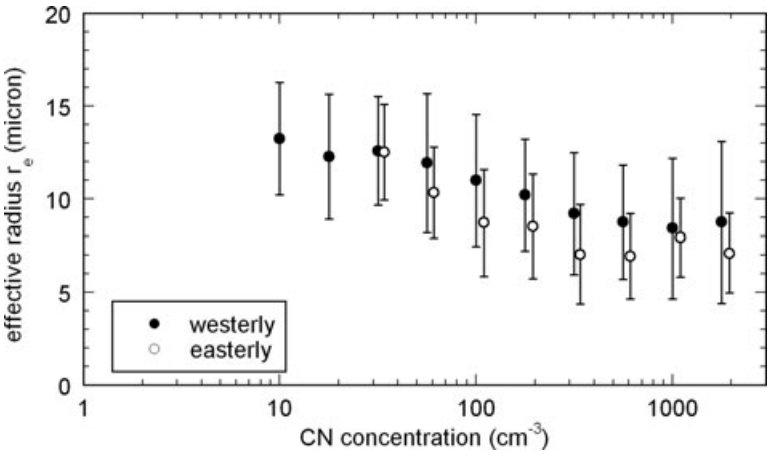

Fig. 5. Instantaneous AERI retrievals of r_e in low-level, optically thin (LWP < 50 g m^{-2}) stratiform cloud cover over Barrow, Alaska, from years 1998–2003 and for the months of July and August, for two prevailing wind regimes, westerly (240–320°) and easterly (20–100°), as a function of corresponding hourly-averaged CN concentration, as in Fig. 4.

Research on the IDE_1 at lower latitudes, where the energy budget is dominated by short-wave radiation, has emphasized the surface cooling by enhanced cloud reflection (Lohmann and Feichter, 2005; Penner et al., 2006) as opposed to the long-wave warming manifestation identified in the Arctic (Garrett and Zhao, 2006; Lubin and Vogelmann, 2006). To determine the total impact of the IDE_1 on the Arctic surface energy budget and climate, we must examine its impact on both short-wave and long-wave radiation. The long-wave surface-warming component of the IDE_1 for thin clouds has been estimated previously at +3.4 W m^{-2} during spring (Lubin and Vogelmann, 2006). Here we observationally determine the short-wave component by using pyranometer measurements of downwelling short-wave surface irradiance simultaneously with the *LWP*s from AERI and MWR data.

Figure 6a shows the difference in T_c between clean-air and all other conditions in four bins encompassing the full range of observed cloud *LWP* in our data from March–May. A decrease in T_c signifies a reduction in short-wave flux at the surface, or a cooling effect. Decreased T_c in the presence of enhanced aerosols appears throughout the data set, and is more statistically significant at higher *LWP*. In contrast, the long-wave manifestation of the springtime IDE_1 occurs only for clouds with *LWP* < ~50 g m^{-2}, since optically thicker clouds radiate essentially as blackbodies (Turner, 2005; Garrett and Zhao, 2006; Lubin and Vogelmann, 2006). June (Fig. 6b) also shows an IDE_1 manifestation, with differences between clean-air and all other conditions appearing as more statistically significant for smaller *LWP*. During July–August (Fig. 6c), statistically significant differences appear for all *LWP*. During September–October (Fig. 6d), there is no evidence of a short-wave manifestation of the IDE_1.

Figure 6 is highly suggestive of a short-wave manifestation of the IDE_1, since the *t*-tests for the various *LWP* bins indicate consistent statistical significance in the differences between the clean-air and the other cases across nearly the full range of *LWP*. However, Fig. 6 is not entirely conclusive because the *LWP* bins are quite wide. In Fig. 7, we perform a more stringent test for persistence of the IDE_1 at constant *LWP* by calculating the average T_c, in both clean-air and all other conditions, in averages of 30 data points about each *LWP* value shown. The result shown in Fig. 7 is conceptually consistent with the IDE_1 if cloud T_c differences are found between clean-air and all other conditions for fixed *LWP*. In both spring and summer, the T_c difference shows a local minimum around *LWP* = 30 g m^{-2}, which is consistent with radiative transfer simulations that indicate the IDE_1 should be harder to detect in surface Arctic data in this moderate *LWP* range (Lubin and Vogelmann, 2007). For all other *LWP* during spring, the T_c difference between clouds under clean-air versus all other conditions is positive and above the instrument detection uncertainty, which signifies a reduction in surface insolation under cloud when CN > 50 cm^{-3}. A similar result is found for optically thinner clouds during summer. This result is less pronounced in June, where T_c differences hover just above or about the detection level for 30 < *LWP* < 80 g m^{-2} and then drop below the detection uncertainty for larger *LWP*. However, during July and August, pronounced T_c differences are found for *LWP* < 100 g m^{-2}, while for larger *LWP* values the differences are consistently less and, in many cases, drop below the detection uncertainty. During autumn the T_c differences are positive but almost entirely below the detection uncertainty, as may be expected from Figs. 4d and 6d.

4. Discussion

These results show observational evidence of a short-wave IDE_1 in the Arctic for all observed cloud *LWP* during spring, and during late summer for *LWP* < 100 g m^{-2}. The summertime result is surprising, given the conventional wisdom that the IDE_1 is an anthropogenic springtime phenomena in the Arctic (Garrett and Zhao, 2006; Lubin and Vogelmann, 2006) and given that aerosol mass concentrations during the Barrow summer are typically —four to five times smaller than in spring (Quinn et al., 2002). However, this summertime result may be valid based the following two considerations. First, Dong and Mace (2003)

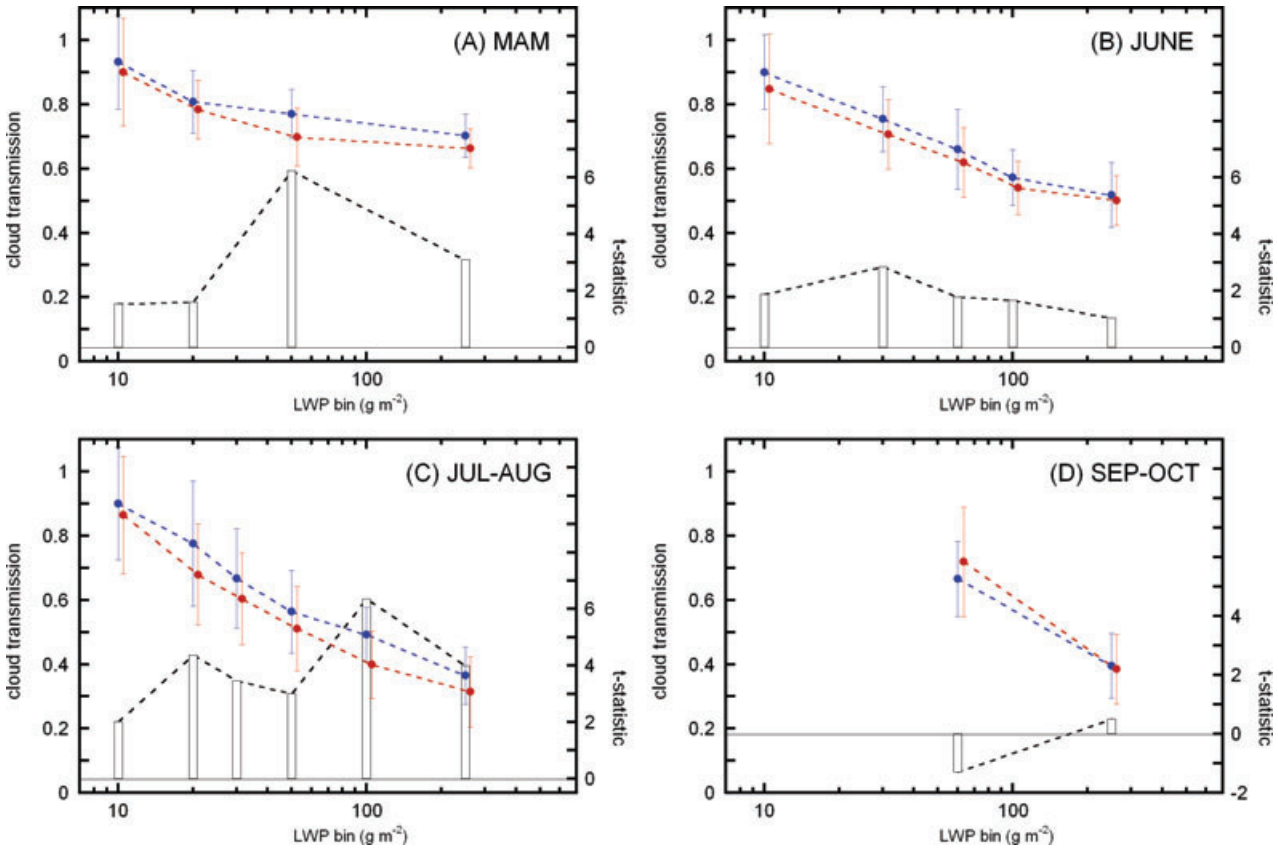

Fig. 6. Cloud transmissions T_c under clean-air (blue; CN < 50 cm^{-3}) and all other conditions (red; CN > 50 cm^{-3}), averaged over all data from (A) March–May (1998–2003), (B) June, (C) July–August and (D) September–October. *LWP* bin ranges are determined by the availability of enough data points ($n \geq 30$) for meaningful statistics: (A) 0–10, 10–20, 20–50 and 50–250 g m^{-2}; (B) 0–10, 10–30, 30–60, 60–100 g m^{-2} and 100–250 g m^{-2}; (C) 0–10, 10–20, 20–30, 30–50, 50–100, 100–250 g m^{-2} and (D) 0–60, 60–250 g m^{-2}. Vertical error bars are $\pm 1\sigma$, and the statistical significance of the average T_c differences between clean-air and all other conditions in each bin are indicated by Student's *t*-test. All T_c values used in this averaging have been normalized to a solar zenith angle of 60° to remove a small but non-negligible solar zenith angle dependence, as described in the text.

used NSA cloud radar, pyranometer and microwave radiometer data to retrieve r_e for NSA clouds, where *LWP* is determined by the microwave radiometer. Their retrievals show r_e in the range 7–10 μm during spring and 10–15 μm during summer. The latter are consistent with our summertime values for clean air in Fig. 4 (CN < 50 cm^{-3}), but are larger than our retrieved r_e under CN > 50 cm^{-3}. We infer from this that summertime aerosol do not affect optically thicker clouds sufficiently to change their climatologically averaged r_e and, hence, the surface radiation balance under them. It remains to be explained why optically thicker clouds appear to be unaffected. Second, a recent study of spring and summertime Arctic aerosol, using well-tested global aerosol and chemical transport models (Korhonen et al., 2008), shows that updraft velocities frequently observed in summertime Arctic boundary layer clouds, of order 15 cm s^{-1} (Lawson et al., 2001), can induce cloud nucleation with the locally produced sulfuric acid particles in the Aitken mode. Arctic Ocean observations of Aitken-mode particles and CCN support this hypothesis (Lohmann and Leck, 2005). Thus, there a plausible mechanism for the summertime IDE$_1$ that we observe primarily in optically thinner clouds. Further, this effect may also represent a negative feedback mechanism (net cooling effect) as the Arctic climate warms, since Gabric et al. (2005) have shown the potential for significant increases in dimethylsulfide (DMS) flux via retreating sea ice cover and warming sea surface temperatures in the Arctic. We note that this summertime effect is at slight variance from the usual definition of IDE$_1$ given by Twomey (1977), who originally described it with reference to pollution aerosol. Here, if the above-described mechanism for the summer IDE$_1$ applies, it manifests from an additional flux of natural particles in a warming climate. Finally, we note that our sample cloud distribution is heavily weighted toward geometrically thin clouds very close to the surface (Fig. 3), and our results concerning to the IDE$_1$ in all seasons pertain only to these clouds and not to cloud cover at higher altitudes. However, Fig. 3, based on 6 yr of ARM data, indicates that thin low level clouds are very frequent in the Arctic in a climatological sense.

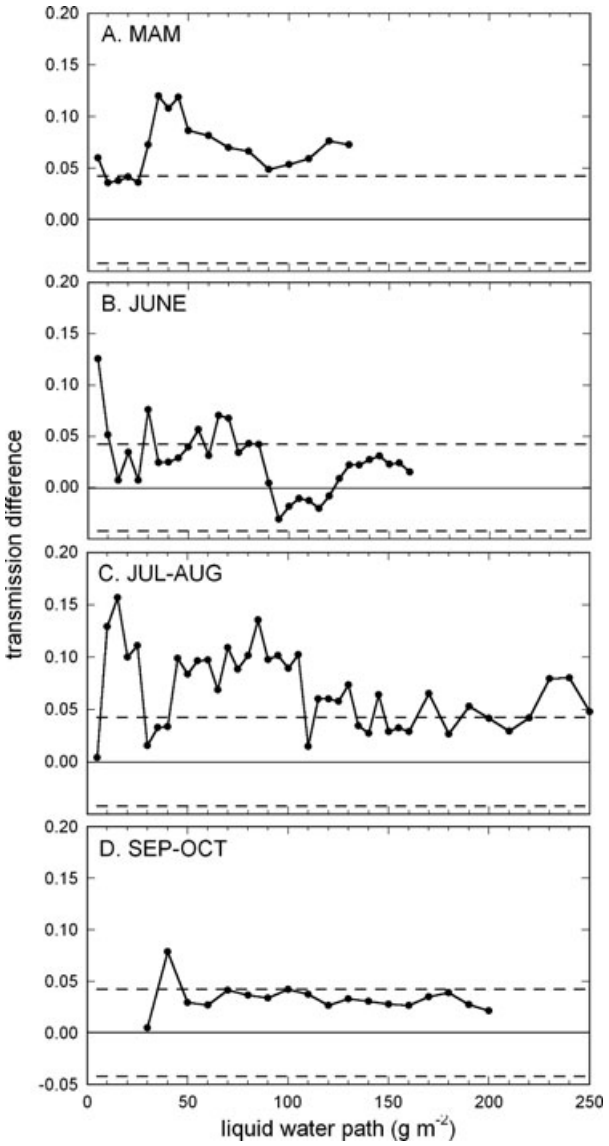

Fig. 7. Cloud transmission differences (clean-air minus all other conditions) evaluated by a moving average constant LWP window for the months (A) March, April and May (MAM), (B) June, (C), July and August and (D) September and October. Each point depicts the difference in mean T_c for the nearest 30 data points having the *LWP* average shown. Dashed lines depict the uncertainty in the T_c difference, which are computed based on the insolation levels at the particular times of year and the ± 5 W m^{-2} uncertainty in pyranometer-measured flux that is estimated for the ARM program's data collection and reduction methods (Michalsky et al., 1999). All T_c values used in this averaging have been normalized to a solar zenith angle of 60° to remove a small but non-negligible solar zenith angle dependence, as described in the text.

Although explanations for our summertime evidence of an IDE_1 can be proposed, we caution that this result remains counterintuitive based on our understanding of the seasonal variation in Arctic aerosol microphysics and chemistry. In demonstrating this result with the available ground-based data, we cannot use CN to determine a threshold for detecting CCN during summer. Instead, we can only use CN to isolate the clean-air cases from all other cases, which may or may not involve CCN. We do not find an obvious airmass correlation artefact in the summertime result when we examine the available surface meteorological data (Fig. 5); however a more extensive backtrajectory analysis of this multiyear NSA data set could be beneficial. At this point, our results suggest that theoretical and field investigations should examine potential manifestations of an IDE_1 during the Arctic summer. However, we do not suggest that the magnitude of the summertime IDE_1 that appears in this study should be taken as a benchmark observation until the result is more fully explained and/or all conceivable artefacts are conclusively eliminated.

In summary, our observations show a short-wave IDE_1 during spring, evidence of a short-wave IDE_1 in cloud with smaller *LWP* during summer, and a barely perceptible IDE_1 during autumn. The autumn result is not surprising given that: (1) during refreeze of the sea ice the above-described DMS particle flux would decrease; (2) the overall aerosol burden is substantially reduced as compared with spring, after several months of removal by precipitation and influence of air masses from lower latitudes and (3) mixed-phase clouds are highly prevalent during autumn in the high Arctic (e.g. Verlinde et al., 2007), which reduces the sample sizes available for the liquid water cloud analysis described herein. Spring holds the greatest interest, due to the enormous seasonal increase in insolation that modulates the surface energy budget just prior to the melt season that often begins in late May (Perovich et al., 2002; also see Fig. 1).

We now estimate the total (short-wave plus long-wave) IDE_1 impact on the surface radiation budget by combining our short-wave result in Fig. 6a with our previous estimate of the long-wave warming from the IDE_1 (Lubin and Vogelmann, 2006) using our radiative transfer model and the observed distribution of springtime Arctic cloud *LWP* at Barrow (Lubin and Vogelmann, 2007). With these data, we calculate the time evolution of the total IDE_1 impact on the downwelling surface radiation budget at Barrow, Alaska and at latitudes farther north (Fig. 8), noting that shipboard transects of cloud observations as far as the pole (Lubin and Simpson, 1997) suggest that stratiform cloud opacities observed from Barrow's latitude are representative of more northerly latitudes as well. At most locations during March, the IDE_1 yields a surface warming. During April, the IDE_1 transitions to a slight cooling, whose magnitude varies with latitude, as the additional insolation attenuated by clouds with smaller r_e begins to exceed the enhanced cloud emission caused by the smaller r_e. Throughout May, surface cooling by the IDE_1 becomes more spatially uniform and its absolute magnitude increases from –7 to –11 W m^{-2}. Because both low-level cloud cover and anthropogenic aerosol are pervasive phenomena throughout the Arctic winter and spring, climate model simulations should account for this aerosol-cloud interaction which yields a climatologically significant surface warming

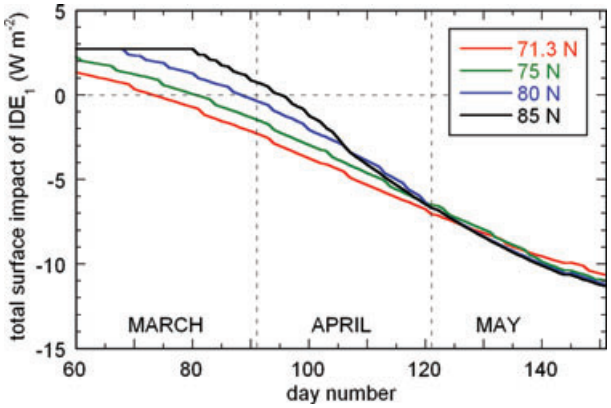

Fig. 8. Time evolution of the springtime total IDE_1 impact on the downwelling surface energy budget, based on the results of Fig. 2, and the climatological *LWP* distributions for low-level Arctic clouds (Lubin and Vogelmann, 2007) and a climatological cloud amount of 80% (Lubin and Vogelmann, 2006). Results are derived using the radiative transfer model for Barrow's latitude (71.3°N) and three higher latitudes. The IDE_1 impact is expressed as the change in diurnally averaged total downwelling surface flux (short-wave plus long-wave) due to an aerosol-induced reduction in r_e. The vertical dashed lines identify April 1 and May 1. Positive (negative) values indicate total surface warming (cooling).

during winter and early spring, followed by surface cooling just prior to the onset of sea ice melt.

5. Acknowledgments

This work was supported by the NSF Arctic Natural Sciences and DOE ARM programs. We thank J. Ogren for access to the NOAA CMDL aerosol data.

References

Clothiaux, E. E., Ackermann, T. P., Mace, G. C., Moran, K. P., Marchand, R. T. and co-authors. 2000. Objective determination of cloud heights and radar reflectivities using a combination of active remote sensors at the ARM CART sites. *J. Appl. Meteorol.*, **39**, 645–665.

Delene, D. J. and Ogren, J. A. 2002. Variability of aerosol optical properties at four North American surface monitoring sites. *J. Atmos. Sci.*, **59**, 1135–1150.

Dong, X. and Mace, G. G. 2003. Arctic stratus cloud properties and radiative forcing derived from ground-based data collected at Barrow, Alaska. *J. Clim.*, **16**, 445–461.

Engvall, A.-C., Krejci, R., Strom, J., Minikin, A., Treffeisen, R. and co-authors. 2008. In-situ airborne observations of the microphysical properties of the Arctic tropospheric aerosol during late summer and spring. *Tellus*, **60B**, 392–404.

Gabric, A. J., Qu, B., Matrai, P. and Hirst, A. C. 2005. The simulated response of dimethylsulfide production in the Arctic Ocean to global warming. *Tellus*, **57B**, 391–403.

Garrett, T. J. and C. Zhao. 2006. Increased Arctic cloud longwave emissivity associated with pollution from mid-latitudes. *Nature*, **440**, 787–789.

Garrett, T. J., Zhao, C., Dong, X., Mace, G. G. and Hobbs, P. V. 2004. Effects of varying aerosol regimes on low-level Arctic stratus. *Geophys. Res. Lett.*, **31**, doi:10.1029/2004GL019928.

Grenfell, T. C. and Perovich, D. K. 1984. Spectral albedos of sea ice and incident solar irradiance in the Southern Beaufort Sea. *J. Geophys. Res.*, **89**, 3573–3580.

Guo, G., Ji, Q., Yang, P. and Tsay, S.-C. 2005. Remote sensing of cirrus optical and microphysical properties from ground-based infrared radiometric measurements – Part II: retrievals from CRYSTAL-FACE measurements. *IEEE Geosci. Rem. Sens. Lett.*, **2**, 132–135.

Heintzenberg, J., Leck, C., Birmili, W., Wehner, B., Tjernström, M. and Weidensohler, A. 2006. Aerosol number-size distributions during clear and fog periods in the summer high Arctic: 1991, 1996 and 2001. *Tellus*, **58B**, 41–50.

Knuteson, R. O., Revercomb, H. E., Best, F. A., Ciganovich, N. C., Dedecker, R. G. and co-authors 2004. Atmospheric Emitted Radiance Interferometer. Part II: instrument performance. *J. Ocean. Atmos. Tech.*, **21**, 1777–1789.

Korhonen, H., Carslaw, K. S., Spracklen, D. V., Ridley, D. A. and Ström, J. 2008. A global model study of processes controlling aerosol size distributions in the Arctic spring and summer. *J. Geophys. Res.*, **113**, doi:10.1029/2007JD009114.

Lawson, R. P., Baker, B. A. and Schmitt, C. G. 2001. An overview of microphysical properties of Arctic clouds observed in May and July 1998 during FIRE ACE. *J. Geophys. Res.*, **106**, 14989–15014.

Lohmann, U. and Feichter, J. 2005. Global indirect aerosol effects: a review. *Atm. Chem. Phys.*, **5**, 715–737.

Lohmann, U. and Leck, C. 2005. Importance of submicron surface-active organic aerosols for pristine Arctic clouds. *Tellus*, **57B**, 261–268.

Lubin, D. and Simpson, A. S. 1997. Measurement of surface radiation fluxes and cloud optical properties during the 1994 Arctic Ocean Section. *J. Geophys. Res.* **102**, 4275–7286.

Lubin, D. and Vogelmann, A. M. 2006. A climatologically significant aerosol longwave indirect effect in the Arctic. *Nature*, **439**, 345–456.

Lubin, D. and Vogelmann, A. M. 2007. Expected magnitude of the aerosol shortwave indirect effect in springtime Arctic liquid water clouds. *Geophys. Res. Lett.*, **34**, L11801, doi:10.1029/2006GL028750.

Mauger, G. and Norris, J. R. 2007. Meteorological bias in satellite estimates of aerosol-cloud relationships. *Geophys. Res. Lett.*, **34**, L16824, doi:10.1029/2007GL029952.

Michalsky, J., Dutton, E., Rubes, M., Nelson, D., Stoffel, T. and co-authors 1999. Optimal measurement of surface shortwave irradiance using current instrumentation. *J. Ocean. Atmos. Tech.*, **16**, 55–69.

Morrison, H., Curry, J. A., Shupe, M. D. and Zuidema, P. 2005. A new double-moment microphysics parameterization for application in cloud and climate models. Part II: single-column modeling of arctic clouds. *J. Atmos. Sci.*, **62**, 1678–1693.

Penner, J. E., Quaas, J., Storelvmo, T., Takemura, T., Boucher, O. and co-authors 2006. Model intercomparison of indirect aerosol effects. *Atmos. Chem. Phys.* **6**, 3391–3405.

Perovich, D. K., Grenfell, T. C., Light, B. and Hobbs, P. V. 2002. Seasonal evolution of the albedo of multiyear Arctic sea ice. *J. Geophys. Res.*, **107**, doi:10.1029/2000JC000438.

Podgorny, I. and Lubin, D. 1998. Biologically active insolation over Antarctic waters: effect of a highly reflecting coastline. *J. Geophys. Res.*, **103**, 2919–2928.

Polissar, A. V. and Hopke, P. K. 2001. Source regions for atmospheric aerosol measured at Barrow, Alaska. *Environ. Sci. Technol.*, **35**, 4214–4226.

Quinn, P. K., Miller, T. L., Bates, T. S., Ogren, J. A., Andrews, E. and co-authors 2002. A 3-year record of simultaneously measured aerosol chemical and optical properties at Barrow, Alaska. *J. Geophys. Res.*, **107**, doi:10.1029/2001JD001248.

Stamnes, K., Tsay, S.-C., Wiscombe, W. J. and Jayaweera, K. 1988. Numerically stable algorithm for discrete-ordinate-method radiative transfer in multiple scattering and emitting layered media. *Appl. Opt.*, **27**, 2502–2509.

Stamnes, K., Ellingson, R. G., Curry, J. A., Walsh, J. E. and Zak, B. D. 1999. Review of science issues, deployment strategy, and status for the ARM North Slope of Alaska–Adjacent Arctic Ocean climate research site. *J. Clim.*, **12**, 46–63.

Stroeve, J., Holland, M. M., Meier, W., Scambos, T. and Serreze, M. C. 2007. Arctic sea ice decline: faster than forecast. *Geophys. Res. Lett*, **34**, L09501, doi:10.1029/2007GL029703.

Turner, D. D. 2005. Arctic mixed-phase cloud properties from AERI lidar observations: algorithm and results from SEHBA. *J. Appl. Meteorol.*, **44**, 427–444.

Twomey, S. 1977. The influence of pollution on the shortwave albedo of clouds. *J. Atmos. Sci.*, **34**, 1149–1152.

Verlinde, J., Harrington, J. Y., McFarquhar, G. M., Yannuzi, V. T., Avaramov, A. and co-authors 2007. The mixed-phase arctic cloud experiment. *Bull. Am. Meteorol. Soc.*, **88**, 205–221.

Westwater, E. R., Han, Y., Shupe, M. D. and Matrosov, S. 2001. Analysis of integrated cloud liquid water and precipitable water vapor retrievals from microwaver radiometers during the Surface Heat Budget of the Arctic Ocean project. *J. Geophys. Res.*, **106**, 32019–32030.